INORGANIC CHEMISTRY FRONTIERS

RESEARCH ARTICLE

View Article Online
View Journal

Cite this: DOI: 10.1039/d5qi00372e

Ultra-small β-Ni(OH)$_2$ quantum dot catalyst with abundant edges for an efficient urea oxidation reaction†

Qishuang Zhu,‡[a] Xianshu Qiao, *‡[a] Chuanjin Tian,[a] Pengzhang Li,[a] Yumin Liu,[a] Wenyan Zhao,[a] Liang Ma[b] and Chang-An Wang *[c]

Received 7th February 2025,
Accepted 15th April 2025

DOI: 10.1039/d5qi00372e

rsc.li/frontiers-inorganic

The development of efficient nonprecious-metal catalysts for the urea oxidation reaction (UOR) to improve the efficiency of electrocatalytic water splitting for hydrogen production remains a challenge. Herein, we synthesized ultra-small β-Ni(OH)$_2$ quantum dot (US-β-Ni(OH)$_2$ QD) catalysts with abundant edges *via* a coupled co-precipitation and anion-exchange approach. The obtained US-β-Ni(OH)$_2$ QD catalyst exhibits high activity toward the UOR and required a potential of only 1.48 V (*vs.* RHE) to reach 151 mA cm^{-2}. Notably, the US-β-Ni(OH)$_2$ QD catalyst exhibits 4.1 and 96 times higher current density than do β-Ni(OH)$_2$ nanosheets (38.34 mA cm^{-2}) and a Pt mesh electrode (1.57 mA cm^{-2}), respectively, at a potential of 1.48 V (*vs.* RHE). The UOR catalytic reaction mechanism reveals that the US-β-Ni(OH)$_2$ QD catalyst features a high density of edge sites, where the oxygen vacancy concentration far exceeds that of the basal plane. This unique oxygen-vacancy-rich edge structure endows the US-β-Ni(OH)$_2$ QDs with a low energy barrier (0.96 eV) for the self-oxidation of Ni(OH)$_2$ to NiOOH, thereby facilitating the rate-determining step of the entire urea degradation process. This work provides a new approach for synthesizing ultra-small hydroxide quantum dot catalysts with efficient UOR activity at low cost.

1. Introduction

Hydrogen energy, a green and clean energy, has become one of the most promising energy resources for humans.[1–3] Hydrogen production *via* water electrolysis has been regarded as a research hotspot owing to its advantages of high conversion efficiency, high product purity, and environmental friendliness.[4–7] Nevertheless, a high thermodynamic potential of 1.23 V required for the anodic OER has severely limited the rate of electrolytic water splitting, making the practical application of electrolytic hydrogen production technology on a large scale challenging for decades.[8–10] It is an effective strategy for reducing the voltage of water electrolysis to utilize small molecule oxidation reactions with a low thermodynamic potential to replace the OER. The thermodynamic potential of the urea oxidation reaction (UOR) requires merely 0.37 V, which makes the UOR a perfect substitute for the OER.[11,12] It not only effectively reduces the cost of hydrogen production but also alleviates the environmental pollution caused by urea-rich wastewater, achieving the dual goals of clean-energy production and environmental protection. However, this advanced technology is limited by the slow UOR kinetics due to the complex 6e$^-$ redox process of the UOR.[13,14] Therefore, highly efficient UOR catalysts are required to improve the kinetically sluggish process for realizing efficient urea oxidation.

To date, precious metal materials such as platinum and ruthenium have shown outstanding electrocatalytic activity for the UOR. However, their high cost and scarcity significantly restrict their large-scale application.[15,16] Hence, it is vital to develop an economical, efficient, and stable nonprecious-metal UOR catalyst. As an important energy material, β-Ni(OH)$_2$ is widely applied in the field of electrocatalysis.[17,18] Research indicates that the conversion of Ni^{2+} into Ni^{3+} on β-Ni(OH)$_2$ surfaces must first take place during the oxidation of urea molecules.[19,20] However, the oxidation potential of the Ni^{2+}/Ni^{3+} reaction is much higher than the standard potential of urea oxidation, and the excessive potential will significantly reduce the energy efficiency of the UOR process.[21] Therefore, it

[a]*School of Materials Science and Engineering, Jingdezhen Ceramic University, Jingdezhen, Jiangxi 333403, P. R. China. E-mail: qiaoxianshu@jcu.edu.cn*
[b]*School of Materials Science and Engineering, Harbin Institute of Technology, Harbin, Heilongjiang 150001, P. R. China*
[c]*School of Materials Science and Engineering, Tsinghua University, Beijing 100010, P. R. China. E-mail: wangca@tsinghua.edu.cn*

†Electronic supplementary information (ESI) available. See DOI: https://doi.org/10.1039/d5qi00372e

‡These authors contributed equally to this work.

is highly desirable to develop β-$Ni(OH)_2$ catalysts featuring a lower onset oxidation potential of the Ni^{2+}/Ni^{3+} reaction for enhancing the performance of urea oxidation.

Activating the Ni-OH bond is an obvious strategy to promote the conversion of Ni^{2+} into Ni^{3+}.[22] Given that the Ni-OH bond of edges in β-$Ni(OH)_2$ is more active than that in the basal plane, the development of a β-$Ni(OH)_2$ catalyst with more abundant edges has become an important research trend. Reducing the size of catalysts is a common strategy to expose more edges.[23,24] For example, Luo *et al.* reported that porous β-$Ni(OH)_2$ nanosheets,[25] exposing a larger edge compared with nonporous β-$Ni(OH)_2$ nanosheets, achieved a current density as high as 298 mA cm^{-2} at 1.82 V (*vs.* RHE). Yang *et al.* fabricated two-dimensional β-$Ni(OH)_2$ nanosheets with a size ranging from 20 to 40 nm,[26] exposing more edges, demonstrating 5.7 times higher current density (142.4 mA cm^{-2}) compared with the β-$Ni(OH)_2$ nanosheets at a potential of 0.6 V (*vs.* Ag/AgCl). Despite these major advances, developing a β-$Ni(OH)_2$ catalyst with more abundant edges remains a challenge.[27,28] Ultra-small β-$Ni(OH)_2$ quantum dots with a smaller size can expose more abundant edges, providing more effective catalytic sites for UORs. However, the preparation of ultra-small quantum dots generally involves complex processes, harsh reaction conditions, or low yields.[29,30] Therefore, it is crucial to develop a simple, mild, and high-yielding synthesis strategy for hydroxide ultra-small quantum dot catalysts.

In this work, we synthesized ultra-small β-$Ni(OH)_2$ quantum dot catalysts (US-β-$Ni(OH)_2$ QDs) with abundant edges *via* a coupled co-precipitation and anion-exchange approach. Benefiting from the ultra-small size of the quantum dots, the US-β-$Ni(OH)_2$ QDs demonstrate high UOR activity, requiring only 1.48 V (*vs.* RHE) to arrive at 151 mA cm^{-2}, which reflects 4.1 and 96 times higher current density compared with the β-$Ni(OH)_2$ nanosheet and Pt mesh electrode, respectively. Experimental and theoretical calculation results indicate that the synthesized US-β-$Ni(OH)_2$ QDs feature a high density of edge sites, where the oxygen vacancy concentration far exceeds that of the basal plane. This unique oxygen-vacancy-rich edge structure endows the US-β-$Ni(OH)_2$ QDs with a low energy barrier (0.96 eV) for the self-oxidation of $Ni(OH)_2$ to NiOOH, thereby accelerating the rate-determining step in the overall urea degradation process. These findings open new possibilities for synthesizing ultra-small hydroxide quantum dots as efficient UOR catalysts and shed light on the development of additional catalysts with enhanced edge activity.

2. Results and discussion

2.1. Synthesis and structural characterization

US-β-$Ni(OH)_2$ QDs were synthesized using a facile coprecipitation method in an ethanol solvent, followed by an anionic exchange method. The synthesis route for US-β-$Ni(OH)_2$ QDs is shown in Fig. 1a. In brief, a nickel oxalate precursor (Fig. S1†) with a nanowire structure (NW-NiC_2O_4) was initially synthesized *via* the coprecipitation method using $Ni(NO_3)_2$ and $H_2C_2O_4$. Subsequently, US-β-$Ni(OH)_2$ QDs were fabricated through the anion exchange method using $C_2O_4^{2-}$ and OH^-. The crystal structure and composition of NW-NiC_2O_4 and US-β-$Ni(OH)_2$ QDs were investigated using XRD and FTIR. As shown in Fig. S2 and S3,† XRD and FTIR results validate that the NW-NiC_2O_4 precursor is a crystalline alcohol compound,[31] which is similar to the crystalline water compound. The XRD result of US-β-$Ni(OH)_2$ QDs presents several broad diffraction peaks at 2θ of 19.2°, 33.06°, 38.54°, 52.1°, 59.05° and 62.7°, corresponding to the (001), (100), (101), (102), (110) and (111) crystal planes of hexagonal β-$Ni(OH)_2$ (JCPDS no. 14-0117), respectively, and no diffraction peaks of residual nickel oxalate could be observed for the as-synthesized US-β-$Ni(OH)_2$ QDs. FTIR results (Fig. S3†) show that the US-β-$Ni(OH)_2$ QD catalyst reveals a sharp peak at 3644 cm^{-1}, which is assigned to the characteristic peak of the non-hydrogen bonded hydroxyl groups ($\gamma_{as}OH$) of β-$Ni(OH)_2$. The two peaks at 3369 cm^{-1} and 1640 cm^{-1} are assigned to the stretching vibration and bending vibration of hydroxyl groups in adsorbed water ($\gamma_{as}H_2O$), respectively.[32–34] No characteristic peaks of nickel oxalate were detected, confirming the absence of residual nickel oxalate or other impurities in the as-synthesized US-β-$Ni(OH)_2$ QDs after the anion exchange process.

The synthesis method for the obtained US-β-$Ni(OH)_2$ QD catalyst offered high yields (Fig. S4†). Tyndall experiment results (Fig. 1b) indicate that the particle size range of US-β-$Ni(OH)_2$ QDs is from 1 to 100 nm. SEM (Fig. 1c) and TEM images (Fig. 1d and e) clearly show that the US-β-$Ni(OH)_2$ QD catalyst presents the typical quantum dot morphology.[35–38] Furthermore, the particle size distribution of US-β-$Ni(OH)_2$ QDs was obtained using Image software, and the result (Fig. 1f) shows that the average diameter of US-β-$Ni(OH)_2$ QDs is around 3 nm, indicating that the US-β-$Ni(OH)_2$ QDs have an ultra-small quantum dot structure. This structure might be attributed to the fact that the crystalline alcohol molecules as interlayer ligands can prevent β-$Ni(OH)_2$ agglomeration during the anion exchange reaction process. The HRTEM image (Fig. 1g) displays clear lattice fringes with a spacing of around 2.33 Å, which are attributed to the (101) planes of the hexagonal β-$Ni(OH)_2$ (JCPDS no. 14-0117). The diffraction ring of the SAED pattern (Fig. 1g inset) reveals the highly polycrystalline nature of the US-β-$Ni(OH)_2$ QDs, for each of the rings can be indexed to the (100), (101), (110), and (201) planes of the β-$Ni(OH)_2$. TEM-EDX spectra (Fig. S5†) show that the US-β-$Ni(OH)_2$ QDs are composed of Ni and O and the substrate copper mesh, and the Ni/O ratio is nearly 1 : 2, indicating that the obtained US-β-$Ni(OH)_2$ QDs have high phase purity. For comparison, β-$Ni(OH)_2$ nanosheet catalysts were also synthesized following a reported method,[39] with detailed preparation procedures given in the Experimental section of the ESI.† TEM characterization (Fig. S6†) of the β-$Ni(OH)_2$ nanosheet catalyst revealed a distinct size difference when compared with the US-β-$Ni(OH)_2$ QDs. The β-$Ni(OH)_2$ nanosheet reveals size in-plane dimensions of ≈50 nm, significantly larger than those of US-β-$Ni(OH)_2$ QDs, indicating that the synthesized US-β-$Ni(OH)_2$ QDs feature a high density of edges.

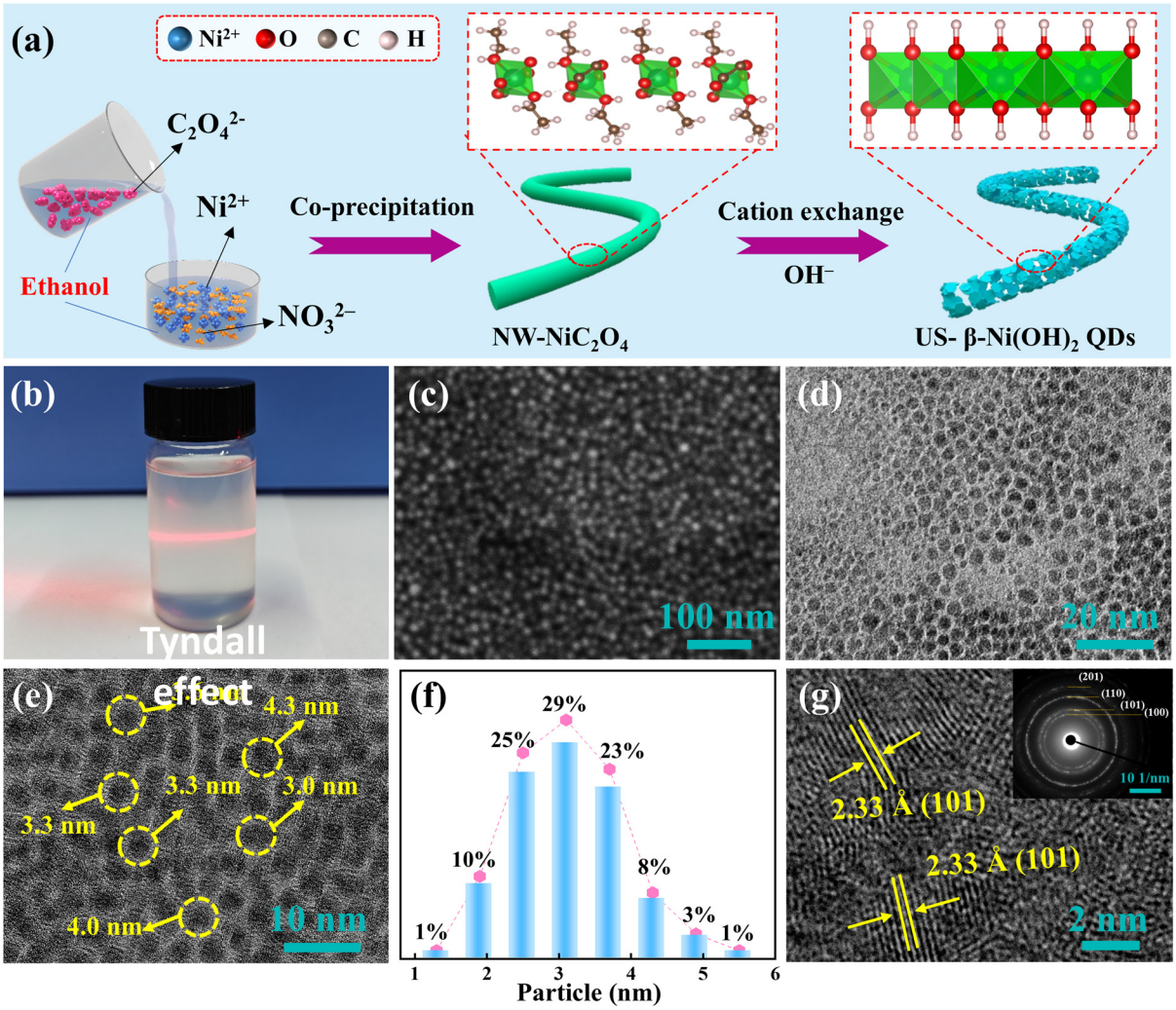

Fig. 1 Synthesis and characterization of US-β-Ni(OH)$_2$ QDs. (a) Schematic of the synthesis of US-β-Ni(OH)$_2$ QDs. (b) Tyndall-effect experiment. (c) SEM image. (d and e) TEM images. (f) The particle size distribution obtained from Image software. (g) HRTEM image and SAED pattern (inset).

To investigate the physical structure differences between US-β-Ni(OH)$_2$ QDs and β-Ni(OH)$_2$ nanosheets, the prepared samples were firstly characterized using XRD measurements (Fig. 2a). XRD results reveal that the diffraction peaks of US-β-Ni(OH)$_2$ QDs are broader than those of β-Ni(OH)$_2$ nanosheets, which can be attributed to the reduced crystallite size. To further investigate size-dependent surface properties, BET measurements were conducted for both samples (Fig. S7†). The results indicate that US-β-Ni(OH)$_2$ QDs exhibit a remarkably high specific surface area of 302.7 m^2 g^{-1}, approximately 2.5 times larger than that of β-Ni(OH)$_2$ nanosheets (122.5 m^2 g^{-1}). This substantial enhancement in the surface area is consistent with the ultra-small dimensions of the quantum dots.

Electron paramagnetic resonance (EPR) spectroscopy was employed to analyze the differences in lattice defects between the US-β-Ni(OH)$_2$ QDs and β-Ni(OH)$_2$ nanosheets. As shown in Fig. 2b, both samples exhibit a significant signal at g = 2.03, suggesting the existence of oxygen vacancies in the two samples. Notably, the US-β-Ni(OH)$_2$ QDs display a substantially enhanced signal intensity at g = 2.03 compared with that of β-Ni(OH)$_2$ nanosheets, indicating a markedly higher concentration of oxygen vacancies in the US-β-Ni(OH)$_2$ QD system. X-ray photoelectron spectroscopy (XPS) analysis provides additional evidence for this finding. XPS survey spectra (Fig. 2c) demonstrate that only Ni and O elements can be detected in both samples, and XPS quantitative analysis reveals a higher Ni/O atomic ratio in US-β-Ni(OH)$_2$ QDs (0.46 : 1) *versus* the nanosheets (0.41 : 1), which is consistent with increased oxygen vacancy concentration. The O 1s peaks for the two samples can be deconvoluted into four peaks at 530.2 eV, 531.0 eV, 531.5 eV, and 532.3 eV, corresponding to the typical metal–oxygen bond (O_L), hydroxyl (O_{OH}) group, oxygen vacancy (O_V), and adsorbed water on the surface (O_W), respectively.[40] The intensity of the O_V signal for the US-β-Ni(OH)$_2$ QDs is stronger than that for the β-Ni(OH)$_2$ nanosheet, further indicating a markedly higher concentration of oxygen vacancies in the US-β-Ni(OH)$_2$ QD system. Ni 2p spectra

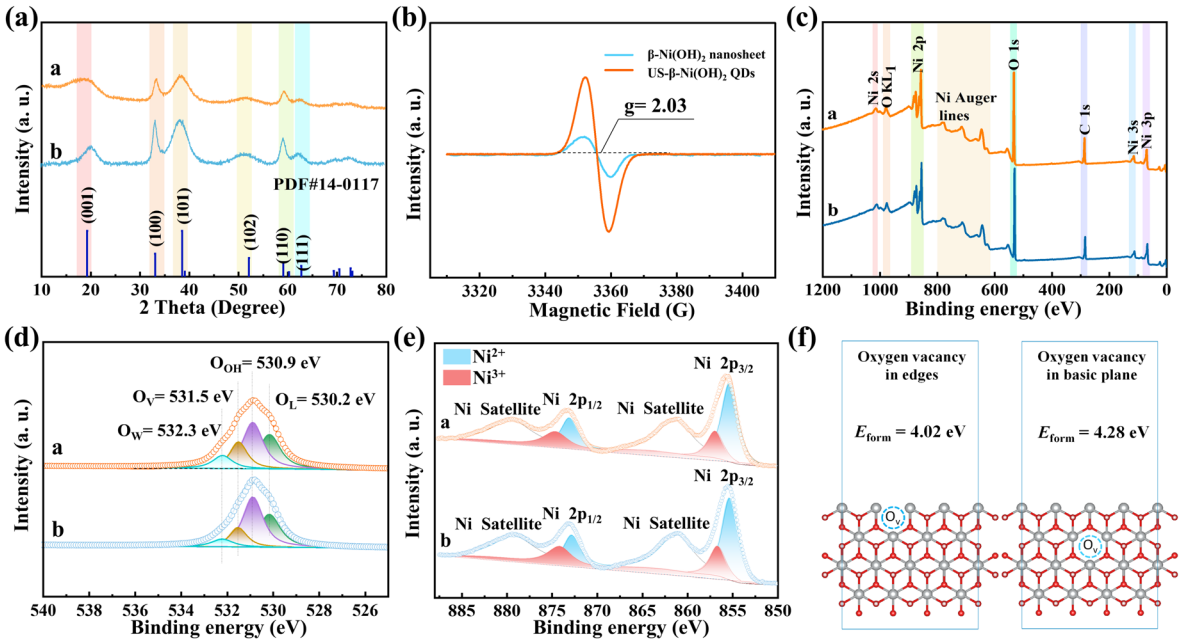

Fig. 2 Structural characterizations of the US-β-$Ni(OH)_2$ QDs (curve a) and β-$Ni(OH)_2$ nanosheet (curve b): (a) XRD patterns. (b) EPR spectrum. (c) XPS survey spectra. (d) O 1s narrow-scan spectra. (e) Ni 2p narrow-scan spectra. (f) Formation energies of V_O at the edge and basal plane sites in β-$Ni(OH)_2$.

(Fig. 2e) of both samples show two main peaks at 856.6 eV and 855.4 eV, corresponding to Ni^{3+} 2p3/2 and Ni^{2+} 2p3/2,[41,42] respectively. The ratio of Ni^{2+}/Ni^{3+} in US-β-$Ni(OH)_2$ QDs is slightly larger than that of β-$Ni(OH)_2$ nanosheets, which likely arises because oxygen vacancies preferentially form at edge sites owing to the low coordination environment of edge oxygen atoms,[43] thereby avoiding substantial alterations in the valence state of Ni. To confirm this viewpoint, DFT calculations were carried out, as shown in Fig. 2f. The results reveal that the formation energy of oxygen vacancies at the edge sites is 4.02 eV, lower than that at the basal plane (4.28 eV), suggesting that oxygen vacancy defects predominantly originate from the edge sites of the β-$Ni(OH)_2$ material.

Based on the above results, it can be concluded that the synthesized US-β-$Ni(OH)_2$ QDs feature a high density of edge sites, where the oxygen vacancy concentration far exceeds that of the basal plane. This unique structural characteristic results in an overall higher concentration of oxygen vacancy defects in the US-β-$Ni(OH)_2$ QDs compared with that in the β-$Ni(OH)_2$ nanosheet catalyst.

2.2. Catalytic activity for the UOR and OER

To survey the electrocatalytic performance of US-β-$Ni(OH)_2$ QDs and β-$Ni(OH)_2$ nanosheets, a series of electrochemical measurements were carried out (Fig. 3). Linear sweep voltammetry (LSV) curves of the two catalysts were collected in 1 M KOH + 0.5 M urea and 1 M KOH solution. As shown in Fig. 3a, the anodic current density of US-β-$Ni(OH)_2$ QDs increases radically as the potential becomes more positive, indicating the impressive electrocatalytic response capacity of US-β-$Ni(OH)_2$ QDs for the UOR. In contrast, a mildly increased anodic current density demonstrates the mediocre catalytic activity of β-$Ni(OH)_2$ nanosheets for the UOR. Specifically, the US-β-$Ni(OH)_2$ QD catalyst delivers a high current density of 151 mA cm^{-2} at an applied potential of 1.48 V (*vs.* RHE), which is roughly 4 and 96 times higher than the values of the β-$Ni(OH)_2$ nanosheets (38.34 mA cm^{-2}) and Pt mesh electrode (1.57 mA cm^{-2}) at the same potential, respectively. The catalytic performance of the US-β-$Ni(OH)_2$ QDs in the UOR was compared with other reported catalysts. From Table S1,† it can be seen that the UOR performance of US-β-$Ni(OH)_2$ QDs demonstrates superior activity compared with most currently available pure nickel-based UOR catalysts, even better than some binary nickel-based UOR catalysts. Moreover, the US-β-$Ni(OH)_2$ QD catalyst shows a higher OER performance (Fig. 3b) compared with β-$Ni(OH)_2$ nanosheets, which exhibit an overpotential of 327 mV at the benchmark 10 mA cm^{-2}. The UOR kinetics of the two catalysts was further investigated using their corresponding Tafel plots. As displayed in Fig. 3c, the Tafel slope value of US-β-$Ni(OH)_2$ QDs is only 22.29 mV dec^{-1}, much lower than that of β-$Ni(OH)_2$ nanosheets (63.61 mV dec^{-1}), signifying its favorable UOR kinetics. In addition, the chronoamperometry curves (Fig. 3d) were collected at a potential of 1.41 V (*vs.* RHE) to examine the durability of US-β-$Ni(OH)_2$ QDs and β-$Ni(OH)_2$ nanosheets. After 20 000 s of durability test, the current density for US-β-$Ni(OH)_2$ QDs only decreased to 98.1% of its initial level, which was higher than that for β-$Ni(OH)_2$ nanosheets, demonstrating the excellent stability of US-β-$Ni(OH)_2$ QDs in the UOR. The longer-time chronopotentiometry curve was also collected at a potential of

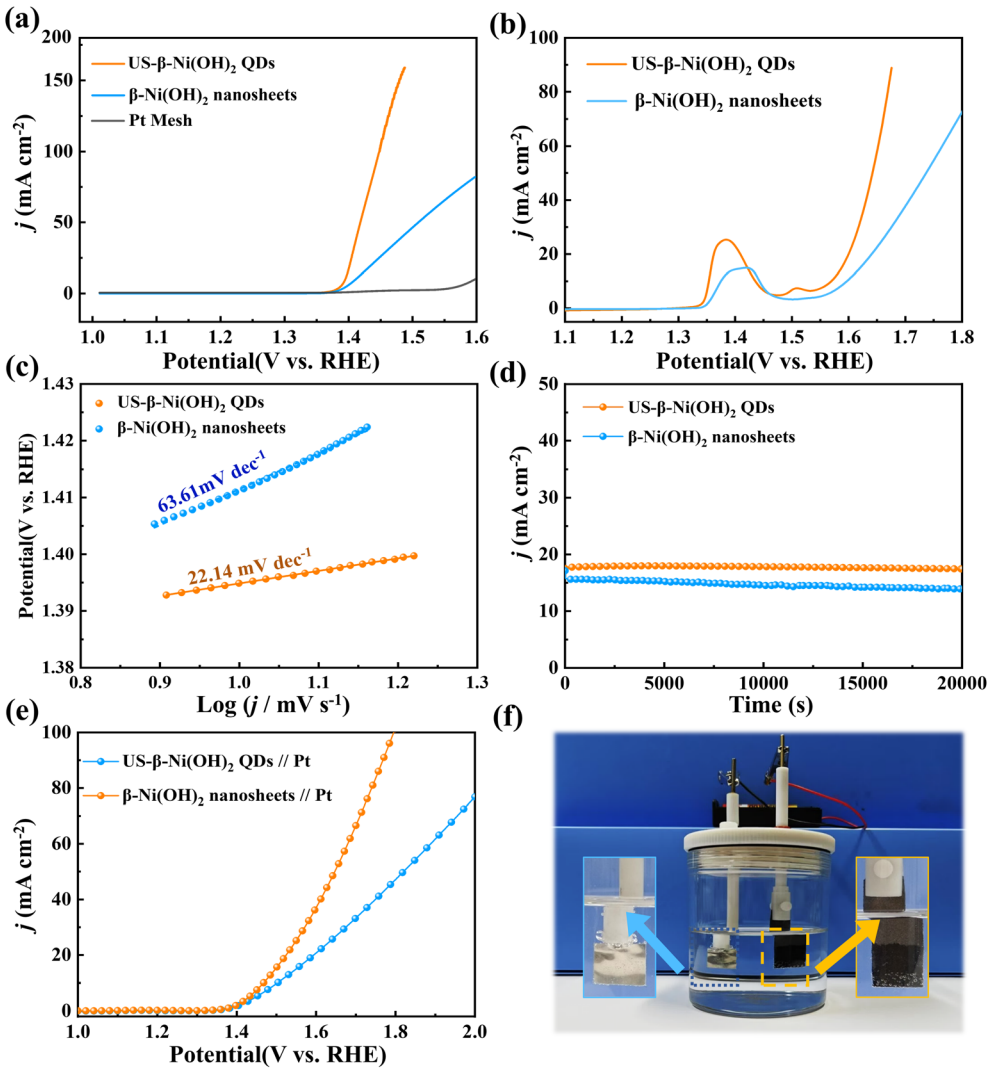

Fig. 3 UOR and OER performance of the as-prepared electrodes. (a) LSV curves for the UOR. (b) LSV curves for the OER. (c) Tafel curves. (d) Durability test at 1.41 V for 20 000 s. (e) LSV curves for urea-assisted water splitting. (f) Urea electrolyzed water driven by a 1.5 V dry battery.

20 mA cm^{-2} to further examine the durability of US-β-$Ni(OH)_2$ QD catalysts. After 20 h of continuous operation, the potential for US-β-$Ni(OH)_2$ QDs only increases to 1% of its initial level (Fig. S8†), further demonstrating the long-term stability of US-β-$Ni(OH)_2$ QDs for the UOR.

Based on the excellent UOR activities and stability of the US-β-$Ni(OH)_2$ QDs, a two-electrode configuration was set up to evaluate the performance of urea-assisted water splitting, wherein a US-β-$Ni(OH)_2$ QDs//Pt mesh cell and β-$Ni(OH)_2$ nanosheet//Pt mesh cell were constructed. As shown in Fig. 3e, the US-β-$Ni(OH)_2$ QDs//Pt mesh cell shows a preferably low working voltage of 1.47 V to attain 10 mA cm^{-2}, preceding β-$Ni(OH)_2$ nanosheets//Pt mesh cell (1.5 V) and indicating an excellent overall catalytic performance for urea electrolysis. Besides, the US-β-$Ni(OH)_2$ QDs//Pt mesh cell was driven by a 1.5 V dry battery (Fig. 3f and Video 1†), and it can be observed that a large number of bubbles are generated in the two electrodes, further indicating the excellent overall water splitting activities of US-β-$Ni(OH)_2$ QDs.

2.3. Mechanism of UOR activity enhancement

As mentioned above, the US-β-$Ni(OH)_2$ QDs show outstanding UOR activity; hence, we examined the mechanism behind the enhanced activity of the US-β-$Ni(OH)_2$ QD catalyst. Firstly, we estimated electrochemical double-layer capacitance (C_{dl}) to determine the real surface area of the catalysts (Fig. 4a and Fig. S9†).

As shown in Fig. 4a, the C_{dl} value of US-β-$Ni(OH)_2$ QDs is 814 μF cm^{-2}, which is significantly higher than that of β-Ni$(OH)_2$ nanosheets (580 μF cm^{-2}), further demonstrating that the reduction of the catalyst size can create more edges, which is a practical way to modulate the electrochemical surface area (ECSA) of β-$Ni(OH)_2$. The increased ECSA induced by increased edges can boost the effective contact between catalysts and

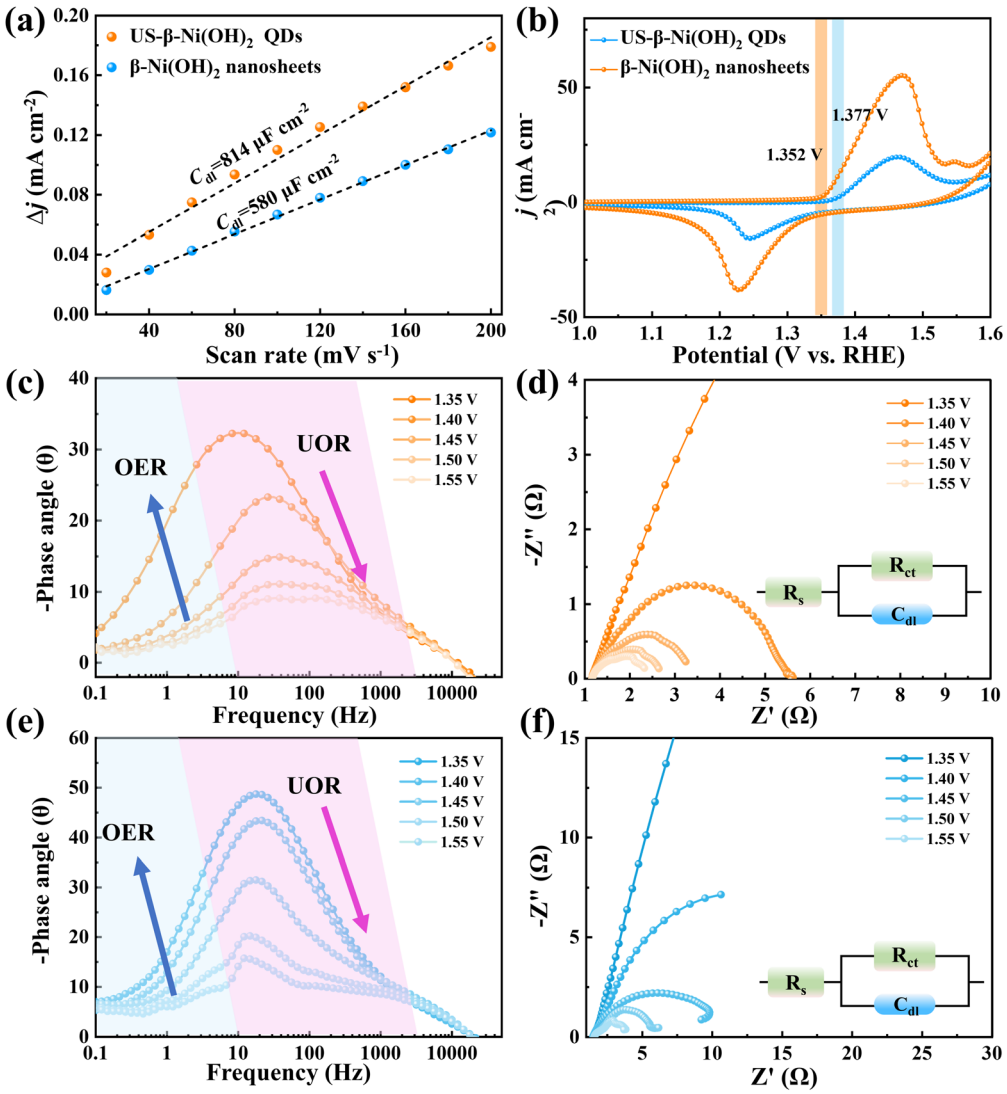

Fig. 4 (a) The calculated C_{dl} values. (b) CV curves collected at the potential ranges from 1.0 V to 1.6 V (*vs.* RHE). Bode plots (c) and Nyquist plots (d) of US-β-Ni(OH)$_2$ QDs. Bode plots (e) and Nyquist plots (f) of the β-Ni(OH)$_2$ nanosheet.

electrolytes, which is conducive to improving the reaction kinetics and the charge transfer capacity at the interface. Furthermore, the polarization curve normalized by C_{dl} is obtained to rule out the influences of the ECSA on the catalytic activity, and the result (Fig. S10†) shows that the inherent activity of US-β-Ni(OH)$_2$ QDs was higher than that of β-Ni(OH)$_2$ nanosheets. To analyze the influences of edges on the catalytic activity of β-Ni(OH)$_2$, CV curves were first plotted at a potential range from 1.0 V to 1.6 V (*vs.* RHE) in 1 M KOH solution. As shown in Fig. 4b, the two catalysts show a couple of redox peaks of Ni^{2+}/Ni^{3+}, and the peaks at around 1.4 V (*vs.* RHE) can be assigned to the electrooxidation of Ni^{2+} to Ni^{3+}. In contrast, the electrooxidation of Ni^{2+} to Ni^{3+} in US-β-Ni(OH)$_2$ QDs occurs beyond 1.352 V, which is earlier than that in β-Ni(OH)$_2$ nanosheets (1.377 V), indicating that the US-β-Ni(OH)$_2$ QDs have a more active Ni^{2+}-OH group than β-Ni(OH)$_2$ nanosheets. Meanwhile, the peak intensity of US-β-Ni(OH)$_2$ QDs is stronger compared with the β-Ni(OH)$_2$ nanosheet, which is mainly because the rich edges with oxygen vacancy are more conducive to generating Ni^{3+}, providing more active sites for the UOR.

Operando electrochemical impedance spectroscopy (EIS) was carried out to further investigate the influence of the electrooxidation of Ni^{2+} to Ni^{3+} on the UOR activity of catalysts. Bode plots of the two catalysts are presented in Fig. 4c and e. To our knowledge, the high-frequency region of Bode plots corresponds to the electrooxidation of Ni^{2+} to Ni^{3+}, and the low-frequency region corresponds to the electrooxidation of Ni^{3+} to Ni^{4+}.[44–47] It can be seen that the peak of US-β-Ni(OH)$_2$ QDs in the high-frequency region is significantly lower than that of β-Ni(OH)$_2$ nanosheets at the same potential, indicating easier oxidation of Ni^{2+} to Ni^{3+}. In addition, the fitting results (Fig. 4d and f) of Nyquist curves reveal that the US-β-Ni(OH)$_2$ QD catalyst exhibits a much lower R_{ct} value than that exhibited

by β-Ni(OH)$_2$ nanosheets at the same potential, suggesting a favorable UOR charge transfer kinetics process.

To investigate the change in the physical and chemical structures of the two catalysts after the UOR, XRD, FTIR, and XPS measurements were performed. After 10 h of the UOR, the XRD result (Fig. 5a) shows that there is almost no change in the diffraction peaks of the two samples, indicating no significant change in their crystal structure after the UOR.

FTIR results (Fig. 5b) of the US-β-Ni(OH)$_2$ QDs and β-Ni(OH)$_2$ nanosheet catalysts after the UOR show two new peaks at 1447 cm^{-1} and 1379 cm^{-1}, which are assigned to the CO_3^{2-} and NO_3^- groups, repectivley.[48,49] Compared with β-Ni(OH)$_2$ nanosheets, the peak intensities of US-β-Ni(OH)$_2$ QDs are lower, primarily owing to the reduced accumulation of toxic byproducts (CO_3^{2-} and NO_3^-) during catalysis, which leads to active site deactivation. To further prove this hypothesis, the chronopotentiometry measurements of the US-β-Ni(OH)$_2$ QDs were performed by separately injecting CO_3^{2-} and NO_3^- solutions to monitor potential changes. After the injection of CO_3^{2-} and NO_3^- solutions, the US-β-Ni(OH)$_2$ QD catalyst presents a reduced activity (Fig. S11†), demonstrating that the accumulation of toxic byproducts (CO_3^{2-} and NO_3^-) can cause activity attenuation. Furthermore, previous studies have confirmed that the oxygen vacancies in Ni(OH)$_2$ can facilitate urea adsorption, thereby inhibiting the deposition of CO_3^{2-} and NO_3^- generated during the UOR and mitigating catalyst poisoning.[50] DFT calculations results (Fig. 5c) reveal that the oxygen vacancies at the edges of β-Ni(OH)$_2$ exhibit a lower urea adsorption energy compared with the V_0-free edge, V_0 at the basal plane, and the basal plane model, further confirming the promoted urea adsorption capability. The US-β-Ni(OH)$_2$ QD catalyst, with its high specific surface area and abundant edge sites, provides more oxygen vacancies for the UOR compared with conventional β-Ni(OH)$_2$ nanosheets. These structural advantages facilitate urea adsorption and prevent the deposition of the formed CO_3^{2-} and NO_3^-; and thus, the stability of US-β-Ni(OH)$_2$ QDs is superior to that of β-Ni(OH)$_2$ nanosheets.

The XPS Ni 2p spectra (Fig. 5d) reveal that the Ni^{2+}/Ni^{3+} ratio in US-β-Ni(OH)$_2$ QDs after the UOR is 1.64, significantly higher than β-Ni(OH)$_2$ nanosheets (1.23), indicating that the oxygen-vacancy-rich edge structure is more conducive to generating Ni^{3+} species, thereby enhancing the UOR process. Meanwhile, the O 1s spectrum (Fig. 5e) shows that the peak

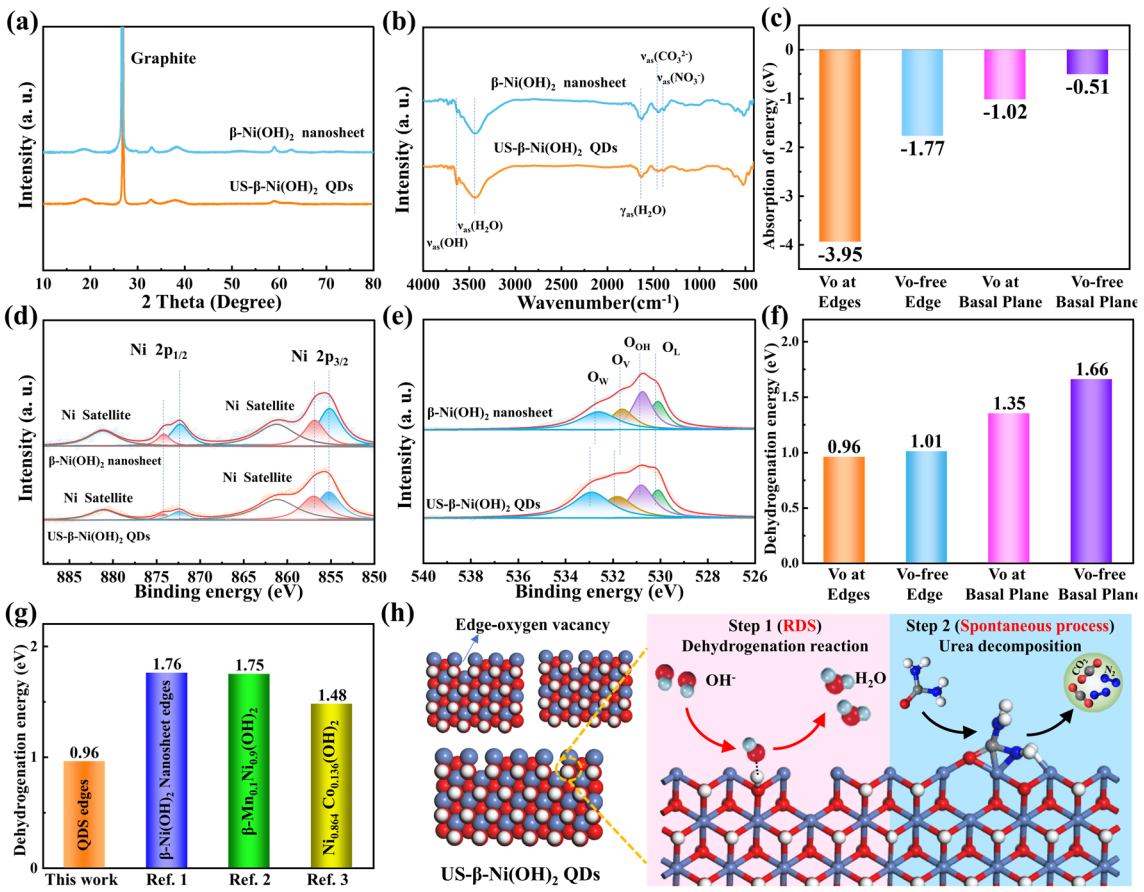

Fig. 5 XRD patterns (a) and FTIR spectra (b) of the US-β-Ni(OH)$_2$ QD and β-Ni(OH)$_2$ nanosheet catalysts after the UOR. (c) Urea adsorption energy of the four distinct configurations. XPS Ni 2p spectra (d) and XPS O 1s spectra (e) of the US-β-Ni(OH)$_2$ QDs and β-Ni(OH)$_2$ nanosheets after the UOR. (f) The dehydrogenation energy of the four distinct configurations. (g) Comparison of dehydrogenation energy with other high-performance UOR catalysts. (h) UOR activity enhancement mechanism schematic for the US-β-Ni(OH)$_2$ QD catalyst.

intensity of adsorbed water (O_W) on the US-β-$Ni(OH)_2$ QD surface after the UOR is markedly stronger than that on β-$Ni(OH)_2$ nanosheets, and the binding energy of O_W for US-β-$Ni(OH)_2$ QDs is higher than for β-$Ni(OH)_2$ nanosheets because the increased Ni^{3+} content not only enhances water molecule adsorption but also elevates the oxidation state of surface oxygen species (O_W).

The UOR of Ni-based materials mainly involves two processes: it begins with the self-oxidation of $Ni(OH)_2$ to NiOOH (the conversion of Ni^{2+} into Ni^{3+}); then, the generated NiOOH spontaneously degrades urea using Ni^{3+} as the catalytic site.[51,52] The dehydrogenation energy, defined as the energy required to remove an H atom from a material, directly corresponds to the Ni^{2+}/Ni^{3+} redox transition. This parameter has been widely recognized as a critical descriptor for assessing UOR activity in nickel-based catalysts. Our theoretical calculations (Fig. 5f) reveal that the dehydrogenation energy for the basal plane of β-$Ni(OH)_2$ is 1.66 eV. Notably, as reported by Wang *et al.*,[53] among the various elementary reactions of urea electrooxidation on the NiOOH surface, the step involving the conversion of the $CONNH_2$ intermediate into CONNH presents the highest energy barrier (1.27 eV). In contrast, the dehydrogenation energy for the basal plane of β-$Ni(OH)_2$ is higher than the value of the $CONNH_2$-to-CONNH conversion energy barrier. This clearly establishes that the conversion of Ni^{2+} into Ni^{3+} is the rate-determining step in the overall urea degradation process. Moreover, the urea adsorption energy of the four configurations is a negative value, which further indicates the spontaneous degradation of urea using Ni^{3+} as the catalytic site. Furthermore, the dehydrogenation energies of the other three distinct configurations were calculated: (i) edge sites incorporating oxygen vacancies; (ii) V_0-free edge sites; and (iii) basal plane sites with oxygen vacancies. The results reveal that edge sites incorporating oxygen vacancies exhibit the lowest dehydrogenation energy (0.96 eV), which is lower than that of the V_0-free edge (1.01 eV), V_0 at the basal plane (1.35 eV), and the basal plane (1.66 eV). This demonstrates that the increased density of edges with oxygen vacancies facilitates the rate-determining step of urea degradation, promoting the oxidation of Ni^{2+} to Ni^{3+} in β-$Ni(OH)_2$. Consequently, the US-β-$Ni(OH)_2$ QDs possess faster reaction kinetics and superior UOR performance compared with conventional β-$Ni(OH)_2$ nanosheets. To contextualize the significance of these findings, the dehydrogenation energy was benchmarked against other high-performance UOR catalysts (Fig. 5g). Notably, the values are substantially lower than those reported for state-of-the-art UOR catalysts, such as β-$Ni(OH)_2$ nanosheet edges (1.76 eV), β-$Mn_{0.1}Ni_{0.9}(OH)_2$ (1.75 eV), and $Ni_{0.864}Co_{0.136}(OH)_2$ (1.48 eV),[26,52,54] further highlighting the exceptional catalytic activity of the US-β-$Ni(OH)_2$ QDs.

To reveal how the lower dehydrogenation energy promotes the Ni^{2+}/Ni^{3+} conversion, the O–H bond length at the β-$Ni(OH)_2$ edges and basal plane were calculated using DFT (Fig. S12†). As shown in Fig. S12,† the O–H bond length at the edge incorporating oxygen vacancies of β-$Ni(OH)_2$ is 0.9421 Å, which is longer than that of V_0-free edge sites, basal plane sites with oxygen vacancies and the basal plane, indicating that the OH group at the edges incorporating oxygen vacancies possess highest chemical reactivity, which can be attributed to the inherently under-coordinated nature of the edge sites of β-$Ni(OH)_2$. The edges with low atomic coordination environments, combined with nearby oxygen vacancies, weakened the O–H bond strength, facilitating proton (H^+) removal from hydroxyl (O–H) groups during the electrochemical process.[55,56]

Based on the above result, the UOR catalytic mechanism of the US-β-$Ni(OH)_2$ QD catalyst was proposed, which is shown in Fig. 5h. During the UOR, the US-β-$Ni(OH)_2$ QD catalyst first undergoes a self-oxidation of $Ni(OH)_2$ to NiOOH (step 1: the conversion of Ni^{2+} into Ni^{3+}); then, the generated NiOOH spontaneously degrades urea using Ni^{3+} as the catalytic site (step 2). The US-β-$Ni(OH)_2$ QD catalyst features a high density of edge sites, where the oxygen vacancy concentration far exceeds that of the basal plane. This structural characteristic significantly reduces the energy barrier for the self-oxidation of $Ni(OH)_2$ to NiOOH by creating more edges with oxygen vacancies, thereby facilitating the rate-determining step of the entire urea degradation process. As a result, the US-β-$Ni(OH)_2$ QDs exhibit faster reaction kinetics and superior UOR performance compared with β-$Ni(OH)_2$ nanosheets.

3. Conclusions

In summary, we synthesized ultra-small β-$Ni(OH)_2$ quantum dot catalysts (US-β-$Ni(OH)_2$ QDs) with abundant edges through the coupling of co-precipitation and anionic exchange. The US-β-$Ni(OH)_2$ QDs demonstrate superior UOR activity, requiring only 1.48 V (*vs.* RHE) to arrive at 151 mA cm^{-2}. Notably, US-β-$Ni(OH)_2$ QDs exhibit 4.1 and 96 times higher current density than do β-$Ni(OH)_2$ nanosheets (38.34 mA cm^{-2}) and the Pt mesh electrode (38.34 mA cm^{-2}) at a potential of 1.48 V (*vs.* RHE), respectively. Experimental and theoretical calculation results indicate that the US-β-$Ni(OH)_2$ QD catalyst features a high density of edge sites, where the oxygen vacancy concentration far exceeds that of the basal plane. This unique oxygen-vacancy-rich edge structure endows the US-β-$Ni(OH)_2$ QDs with a low energy barrier (0.96 eV) for the self-oxidation of $Ni(OH)_2$ to NiOOH, thereby facilitating the rate-determining step of the entire urea degradation process. As a result, the US-β-$Ni(OH)_2$ QDs exhibit faster reaction kinetics and superior UOR performance compared with β-$Ni(OH)_2$ nanosheets. These discoveries provide promising perspectives for the fabrication of hydroxide ultra-small quantum dot catalysts with efficient UOR activities and offer insights for exploring other catalysts with abundant edge activities.

Author contributions

Qishuang Zhu participated in the synthesis and characterization of the compounds and in writing the original draft. Liang Ma assisted with testing, data analysis and graph

drawing. Chuanjin Tian, Pengzhang Li, Yumin Liu and Wenyan Zhao participated in the software-based analysis, formal analysis and funding acquisition. Xianshu Qiao and Chang-An Wang designed the project, supervised and provided helpful discussions, and revised the manuscript.

Data availability

Data will be made available upon request.

Conflicts of interest

The authors declare no competing financial interest.

Acknowledgements

The financial supports of the National Natural Science Foundation of China (no. 52262033), the Natural Science Foundation of Jiangxi Province (no. 20232ACB214004, 20232ACB204011, 20224BAB204001, and 20224BAB214004), the Doctoral Research Initiation Fund of Jingdezhen Ceramic University (Grant No. 20298168), and the Major Research Program of Jingdezhen Ceramic Industry (no. 2023ZDGG001) are greatly appreciated.

References

1 J. Zhang, X. Sheng, Z. Y. Ding, H. L. Wang, L. Feng, X. Q. Zhang, L. P. Wen, L. Jiang and X. J. Feng, Decoupling hydrogen production from water oxidation by integrating a triphase interfacial bioelectrochemical cascade reaction, *Sci. Bull.*, 2021, **66**(2), 164–169.

2 X. A. Teng, Z. B. Wang, Y. S. Wu, Y. Zhang, B. Yuan, Y. Y. Xu, R. M. Wang and A. X. Shan, Enhanced alkaline hydrogen evolution reaction of MoO_2/Ni_3S_2 nanorod arrays by interface engineering, *Nano Energy*, 2024, **122**, 109299.

3 Y. Zheng, Y. Jiao, A. Vasileff and S. Z. Qiao, The hydrogen evolution reaction in alkaline solution: from theory, single crystal models, to practical electrocatalysts, *Angew. Chem., Int. Ed.*, 2018, **57**(26), 7568–7579.

4 A. Hanan, M. N. Lakhan, R. Walvekar, M. Khalid and C. Prakash, Heteroatom-doped MXenes as electrocatalysts for hydrogen evolution reaction: A review on the recent advances, mechanisms and prospects, *Chem. Eng. J.*, 2024, **483**, 149107.

5 S. Q. Zhu, X. Z. Liu, X. S. Wang, Q. L. Zhao and M. H. Shao, Some remaining puzzles in hydrogen electrocatalysis mechanisms on platinum surfaces, *Joule*, 2024, **8**, 1890–1918.

6 L. Ouyang, X. He, Y. T. Sun, L. C. Zhang, D. L. Zhao, S. J. Sun, Y. S. Luo, D. D. Zheng, A. M. Asiri, Q. Liu, J. X. Zhao and X. P. Sun, RuO_2 nanoparticle-decorated TiO_2 nanobelt array as a highly efficient electrocatalyst for the hydrogen evolution reaction at all pH values, *Inorg. Chem. Front.*, 2022, **9**(24), 6602–6607.

7 J. L. Huang, Z. K. Shi, C. W. Mao, G. X. Yang and Y. Chen, Wood–structured nanomaterials as highly efficient, self–standing electrocatalysts for water splitting, *Small*, 2024, 2402511.

8 D. H. Li, N. Shi, Y. J. Wang, P. W. Cai, Y. Q. Sun and S. T. Zheng, An organic–inorganic hybrid polyoxoniobate decorated by a Co(III)-amine complex for electrocatalytic urea splitting, *Inorg. Chem. Front.*, 2023, **10**(16), 4789–4796.

9 J. Wei, Y. F. Shao, J. B. Xu, F. Yin, Z. J. Li, H. T. Qian, Y. P. Wei, L. Chang, Y. Han, J. Li and L. Gan, Sequential oxygen evolution and decoupled water splitting via electrochemical redox reaction of nickel hydroxides, *Nat. Commun.*, 2024, **15**(1), 9012.

10 M. Li, X. H. Deng, Y. Liang, K. Xiang, D. Wu, B. Zhao, H. P. Yang, J. L. Luo and X. Z. Fu, CoxP@ NiCo-LDH heteronanosheet arrays as efficient bifunctional electrocatalysts for co-generation of value-added formate and hydrogen with less-energy consumption, *J. Energy Chem.*, 2020, **50**, 314–323.

11 S. Xu, D. X. Jiao, X. W. Ruan, Z. Y. Jin, Y. Qiu, J. C. Fan, L. Zhang, W. T. Zheng and X. Q. Cui, Synergistic modulation of the d-band center in Ni_3S_2 by selenium and iron for enhanced oxygen evolution reaction (OER) and urea oxidation reaction (UOR), *J. Colloid Interface Sci.*, 2024, **671**, 46–55.

12 H. Z. Xu, K. Ye, K. Zhu, Y. Y. Gao, J. L. Yin, J. Yan, G. L. Wang and D. X. Cao, Hollow bimetallic selenide derived from a hierarchical MOF-based Prussian blue analogue for urea electrolysis, *Inorg. Chem. Front.*, 2021, **8**(11), 2788–2797.

13 H. N. Sun, J. P. Liu, H. Kim, S. Z. Song, L. S. Fei, Z. W. Hu, H. J. Lin, C. T. Chen, F. Ciucci and W. Jung, Ni–doped CuO nanoarrays activate urea adsorption and stabilizes reaction intermediates to achieve high–performance urea oxidation catalysts, *Adv. Sci.*, 2022, **9**(34), 2204800.

14 Y. H. Feng, N. Ran, X. L. Wang, Q. A. Liu, J. C. Wang, L. J. Liu, K. Suenaga, W. W. Zhong, R. G. Ma and J. J. Liu, Nanoparticulate WN/Ni_3C coupling in ceramic coatings for boosted urea electro–oxidation, *Adv. Energy Mater.*, 2023, **13**(42), 2302452.

15 Z. H. Zhang, Z. R. Yu, Y. Zhang, A. Barras, A. Addad, P. Roussel, L. C. Tang, M. Naushad, S. Szunerits and R. Boukherroub, Construction of desert rose flower-shaped NiFe LDH-Ni_3S_2 heterostructures via seawater corrosion engineering for efficient water-urea splitting and seawater utilization, *J. Mater. Chem. A*, 2023, **11**(36), 19578–19590.

16 A. A. Feidenhansl, Y. N. Regmi, C. Wei, D. Xia, J. Kibsgaard and L. A. King, Precious metal free hydrogen evolution catalyst design and application, *Chem. Rev.*, 2024, **124**(9), 5617–5667.

17 K. Y. Zhu, H. Y. Liu, M. R. Li, X. N. Li, J. H. Wang, X. F. Zhu and W. S. Yang, Atomic-scale topochemical preparation of crystalline Fe^{3+}-doped β-$Ni(OH)_2$ for an ultrahigh-rate oxygen evolution reaction, *J. Mater. Chem. A*, 2017, **5**(17), 7753–7758.

18 W. Chen, L. T. Xu, X. R. Zhu, Y. C. Huang, W. Zhou, D. D. Wang, Y. Y. Zhou, S. Q. Du, Q. L. Li, C. Xie, L. Tao, C. L. Dong, J. L. Liu, Y. Y. Wang, R. Chen, H. Su, C. Chen, Y. Q. Zou, Y. F. Li, Q. H. Liu and S. Y. Wang, Unveiling the electrooxidation of urea: intramolecular coupling of the N–N bond, *Angew. Chem., Int. Ed.*, 2021, **60**(13), 7297–7307.

19 H. P. Liu, P. K. Wang, X. Qi, A. Qi, A. Yin, Y. X. Wang, Y. Ye, J. J. Luo, Z. Q. Ren, L. N. Chen, S. Z. Yu and J. Wei, Insights into the understanding of the nickel-based pre-catalyst effect on urea oxidation reaction activity, *Molecules*, 2024, **29**(14), 3321.

20 P. Guo, S. F. Cao, W. J. Huang, X. Q. Lu, W. Z. Chen, Y. Z. Zhang, Y. J. Wang, X. Xin, R. Q. Zou, S. B. Liu and X. H. Li, Heterojunction–induced rapid transformation of Ni^{3+}/Ni^{2+} sites which mediates urea oxidation for energy–efficient hydrogen production, *Adv. Mater.*, 2024, **36**(18), 2311766.

21 Y. Li, M. H. Fan, B. Yu, C. H. Wang, X. Yu, J. Ding, G. Qin, L. Yan, K. Yin and L. L. Wang, Amorphous molybdenum sulfide nanosheets composed of $[Mo_3S_{13}]^{2-}$ active-site motifs for enhancing conversion of Fe^{3+}/Fe^{2+} in Fenton reaction under neutral condition, *Chem. Eng. J.*, 2024, **495**, 153463.

22 W. Chen, Y. Y. Wang, B. B. Wu, J. Q. Shi, Y. Y. Li, L. T. Xu, C. Xie, W. Zhou, Y. C. Huang, T. H. Wang, S. Q. Du, M. L. Song, D. D. Wang, C. Chen, J. Y. Zheng, J. L. Liu, C. L. Dong, Y. Q. Zou, J. Chen and S. Y. Wang, Activated Ni-OH bonds in a catalyst facilitates the nucleophile oxidation reaction, *Adv. Mater.*, 2022, **34**(27), 2105320.

23 P. Xu, C. Y. Tao, Y. Y. Jiang, S. S. Chu, K. P. Song and Y. Z. Lu, Concave single-atom Co nanozymes with densely edge-hosted active sites for highly sensitive immunoassay, *Chem. Eng. J.*, 2024, **495**, 153479.

24 H. B. Zhang, Z. J. Ma, J. J. Duan, H. M. Liu, G. G. Liu, T. Wang, K. Chang, M. Li, L. Shi, X. G. Meng, K. C. Wu and J. H. Ye, Active sites implanted carbon cages in core-shell architecture: highly active and durable electrocatalyst for hydrogen evolution reaction, *ACS Nano*, 2016, **10**(1), 684–694.

25 W. L. Yang, X. P. Yang, B. J. Li, J. H. Lin, H. T. Gao, C. M. Hou and X. L. Luo, Ultrathin nickel hydroxide nanosheets with a porous structure for efficient electrocatalytic urea oxidation, *J. Mater. Chem. A*, 2019, **7**(46), 26364–26370.

26 W. L. Yang, X. P. Yang, C. M. Hou, B. J. Li, H. T. Gao, J. H. Lin and X. L. Luo, Rapid room-temperature fabrication of ultrathin $Ni(OH)_2$ nanoflakes with abundant edge sites for efficient urea oxidation, *Appl. Catal., B*, 2019, **259**, 118020.

27 L. Xue, S. Li, T. Shen, M. Z. Ni, C. Qiu, S. Sun, H. Geng, X. H. Zhu and H. Xia, Two-dimensional metal (oxy) hydroxide and oxide ultrathin nanosheets via liquid phase epitaxy, *Energy Storage Mater.*, 2020, **32**, 272–280.

28 T. Y. Kou, S. W. Wang, J. L. Hauser, M. P. Chen, S. R. J. Oliver, Y. F. Ye, J. H. Guo and Y. Li, Ni foam-supported Fe-doped β-$Ni(OH)_2$ nanosheets show ultralow overpotential for oxygen evolution reaction, *ACS Energy Lett.*, 2019, **4**(3), 622–628.

29 J. Park, A. Jayaraman, A. W. Schrader, G. W. Hwang and H. S. Han, Controllable modulation of precursor reactivity using chemical additives for systematic synthesis of high-quality quantum dots, *Nat. Commun.*, 2020, **11**(1), 5748.

30 Y. S. Park, J. Lim and V. I. Klimov, Asymmetrically strained quantum dots with non-fluctuating single-dot emission spectra and sub-thermal room-temperature linewidths, *Nat. Mater.*, 2019, **18**(3), 249–255.

31 X. S. Qiao, H. J. Kang, Y. Li, K. Cui, X. Jia, X. H. Wu and W. Qin, Novel FeNi–based nanowires network catalyst involving hydrophilic channel for oxygen evolution reaction, *Small*, 2022, **18**(10), 2106378.

32 S. Corsetti, F. M. Zehentbauer, D. McGloin and J. Kiefer, Characterization of gasoline/ethanol blends by infrared and excess infrared spectroscopy, *Fuel*, 2015, **141**, 136–142.

33 M. Casas-Cabanas, M. D. Radin, J. Kim, C. P. Grey, A. Van der Ven and M. R. Palacín, The nickel battery positive electrode revisited: stability and structure of the β-NiOOH phase, *J. Mater. Chem. A*, 2018, **6**(39), 19256–19265.

34 B. Shruthi, V. B. Raju and B. J. Madhu, Synthesis, spectroscopic and electrochemical performance of pasted β-nickel hydroxide electrode in alkaline electrolyte, *Spectrochim. Acta, Part A*, 2015, **135**, 683–689.

35 H. Huang, Y. Xue, Y. Xie, Y. Yang, L. Yang, H. He and G. Ying, MoS_2 quantum dot-decorated MXene nanosheets as efficient hydrogen evolution electrocatalysts, *Inorg. Chem. Front.*, 2022, **9**, 1171–1178.

36 Y. Liang, W. Xu, J. Fang, Z. Liu, D. Chen, T. Pan and Z. Fang, Highly dispersed bismuth oxide quantum dots/graphite carbon nitride nanosheets heterojunctions for visible light photocatalytic redox degradation of environmental pollutants, *Appl. Catal., B*, 2021, **295**, 120279.

37 T. Chiba, Y. Hayashi, H. Ebe, K. Hoshi, J. Sato, S. Sato and J. Kido, Anion-exchange red perovskite quantum dots with ammonium iodine salts for highly efficient light-emitting devices, *Nat. Photonics*, 2018, **12**, 681–687.

38 P. Sun, Z. Xing, Z. Li and W. Zhou, Recent advances in quantum dots photocatalysts, *Chem. Eng. J.*, 2023, **458**, 141399.

39 H. Zhou, J. B. Peng, X. L. Qiu, Y. S. Gao, L. M. Lu and W. M. Wang, β-$Ni(OH)_2$ nanosheets: an effective sensing platform for constructing nucleic acid-based optical sensors, *J. Mater. Chem. A*, 2017, **5**(35), 7426–7432.

40 G. Wang, Z. Yan, M. Xiang, Y. Ding, J. Chen and Z. Xu, Versatile Mo-doped $Ni(OH)_2$/carbon cloth integral electrode: Oxygen vacancy enrichment and conductivity enhancement for high-performance supercapacitor and methanol electrooxidation, *Mater. Today Chem.*, 2024, **42**, 102358.

41 C. L. Huo and H. M. Yang, Attachment of nickel oxide nanoparticles on the surface of palygorskite nanofibers, *J. Colloid Interface Sci.*, 2012, **384**, 55–60.

42 H. A. Hassanin and A. Taha, Sonochemical-assisted biogenic synthesis of theophrasite β-$Ni(OH)_2$ nanocluster using chia seeds extract: Characterization and anticancer activity, *Nanomaterials*, 2022, **12**, 1919.

43 Y. Ye, Y. Gan, R. Cai, X. Dai, X. Yin, F. Nie and X. Zhang, Oxygen vacancies and surface reconstruction on NiFe LDH@$Ni(OH)_2$ heterojunction synergistically triggering oxygen evolution and urea oxidation reaction, *J. Alloys Compd.*, 2022, **921**, 166145.

44 K. Krishnamoorthy, G. K. Veerasubramani, S. Radhakrishnan and S. J. Kim, One pot hydrothermal growth of hierarchical nanostructured Ni_3S_2 on Ni foam for supercapacitor application, *Chem. Eng. J.*, 2014, **251**, 116–122.

45 X. J. Zhang, D. Qi, C. C. Jiao, X. P. Liu and G. S. Zhang, Nickel-catalyzed deaminative sonogashira coupling of alkylpyridinium salts enabled by NN_2 pincer ligand, *Nat. Commun.*, 2021, **12**(1), 4904.

46 J. Cornella, J. T. Edwards, T. Qin, S. Kawamura, J. Wang, C. M. Pan, R. Gianatassio, M. Schmidt, M. D. Schmidt, M. D. Eastgate and P. S. Baran, Practical Ni-catalyzed aryl–alkyl cross-coupling of secondary redox-active esters, *J. Am. Chem. Soc.*, 2016, **138**(7), 2174–2177.

47 Y. J. Wang, W. L. Chen, L. Chen, X. T. Zheng, S. S. Xu and E. B. Wang, Sandwich-type silicotungstate modified TiO_2 microspheres for enhancing light harvesting and reducing electron recombination in dye-sensitized solar cells, *Inorg. Chem. Front.*, 2017, **4**(3), 559–565.

48 C. Liu, L. Xu, J. Deng, Z. Han, Y. Li, J. Wu and J. Fang, Exploring the mechanism of a novel cationic surfactant in bastnaesite flotation via the integration of DFT calculations, *in situ* AFM and electrochemistry, *Int. J. Min. Sci. Technol.*, 2024, **34**(10), 1475–1484.

49 M. Pooresmaeil and H. Namazi, D-mannose functionalized MgAl-LDH/Fe-MOF nanocomposite as a new intelligent nanoplatform for MTX and DOX co-drug delivery, *Int. J. Pharm.*, 2022, **625**, 122112.

50 Z. Zhao, Q. Shao, J. Xue, B. Huang, Z. Niu, H. Gu and J. Lang, Multiple structural defects in ultrathin NiFe-LDH nanosheets synergistically and remarkably boost water oxidation reaction, *Nano Res.*, 2022, **15**, 310–316.

51 J. Tang, Z. Li, H. Jang, X. Gu, C. Sun, M. G. Kim and X. Liu, Local charge modulation induced the formation of high–valent nickel sites for enhanced urea electrolysis, *Adv. Energy Mater.*, 2024, **14**(41), 2403004.

52 W. Chen, C. Xie, Y. Wang, Y. Zou, C. L. Dong, Y. C. Huang, Z. Xiao, Z. Wei, S. Du, C. Chen, B. Zhou, J. Ma and S. Wang, Activity origins and design principles of nickel-based catalysts for nucleophile electrooxidation, *Chem*, 2020, **6**, 2974–2993.

53 X. Zhang, S. Feizpoor, M. Humayun and C. Wang, Urea oxidation reaction electrocatalysts: Correlation of structure, activity, and selectivity, *Chem. Catal.*, 2024, **4**(2), 100840.

54 Z. Zheng, D. Wu, L. Chen, S. Chen, H. Wan, G. Chen and R. Ma, Collaborative optimization of thermodynamic and kinetic for Ni-based hydroxides in electrocatalytic urea oxidation reaction, *Appl. Catal., B*, 2024, **340**, 123214.

55 J. Chen, Y. Shi, S. Zheng, W. Zhao, R. Li, K. Ye and X. Yang, Blocking interfacial proton transport via self–assembled monolayer for hydrogen evolution–free zinc batteries, *Angew. Chem.*, 2024, **136**(26), e202404825.

56 Z. C. Yao, J. Chai, T. Tang, L. Ding, Z. Jiang, J. Fu and L. J. Wan, Manipulating hydrogenation pathways enables economically viable electrocatalytic aldehyde-to-alcohol valorization, *Proc. Natl. Acad. Sci. U. S. A.*, 2025, **122**(8), e2423542122.